Chum et al. Earth, Planets and Space (2016) 68:24
DOI 10.1186/s40623-016-0401-9

Earth, Planets and Space
a SpringerOpen Journal

FULL PAPER Open Access

Ionospheric signatures of the April 25, 2015 Nepal earthquake and the relative role of compression and advection for Doppler sounding of infrasound in the ionosphere

Jaroslav Chum[1*], Jann-Yenq Liu[2], Jan Laštovička[1], Jiří Fišer[1], Zbyšek Mošna[1], Jiří Baše[1] and Yang-Yi Sun[2]

Abstract

Ionospheric signatures possibly induced by the Nepal earthquake are investigated far outside the epicentral region in Taiwan (~3700 km distance from the epicenter) and in the Czech Republic (~6300 km distance from the epicenter). It is shown that the ionospheric disturbances were caused by long period, ~20 s, infrasound waves that were excited locally by vertical component of the ground surface motion and propagated nearly vertically to the ionosphere. The infrasound waves are heavily damped at the heights of F layer at around 200 km, so their amplitude strongly depends on the altitude of observation. In addition, in the case of continuous Doppler sounding, the value of the Doppler shift depends not only on the advection (up and down motion) of the reflecting layer but also on the compression/rarefaction of the electron gas and hence on the electron density gradient. Consequently, under significant differences of reflection height of sounding radio waves and partly also under large differences in plasma density gradients, the observed ionospheric response at larger distances from the epicenter can be comparable with the ionospheric response observed at shorter distances, although the amplitudes of causative seismic motions differ by more than one order of magnitude.

Keywords: Infrasound, Seismic waves, Ionosphere, Wave propagation, Remote sensing

Introduction

The M 7.8 April 25 2015 earthquake occurred in Nepal at 06:11:26 UT. The epicenter was located at (28.147° N, 84.708° E) with estimated depth of about 8.2 km (http://earthquake.usgs.gov/earthquakes; accessed 10 September 2015). The earthquake ruptured a 120 by 50 km shallow dipping midcrustal segment of the Main Himalayan Thrust, the plate boundary fault between the India plate and Tibetan plateau. The rupture propagated during 50 s from its epicenter, located at about 80 km NW of Kathmandu, Nepal's capital city, towards the eastern end situated about 80 km NE of Kathmandu (Avouac et al. 2015; Grandin et al. 2015; Kobayashi et al. 2015; Takai et al. 2016). It has been the largest earthquake in that area since 1934 with a number of casualties and destroyed buildings, including historical monuments. The ground motion was also responsible for the large disturbances in the ionosphere.

Investigation of co-seismic disturbances in the ionosphere started about 50 years ago [Bolt 1964; Donn and Posmentier 1964; Davies and Baker 1965]. It is generally accepted that vertical motion of the ground surface causes pressure changes in the atmosphere which then propagate upwards as acoustic gravity waves [Le Pichon et al. 2002; Artru et al. 2004; Watada et al. 2006; Chum et al. 2012]. Only strong earthquakes which generate seismic waves with sufficiently long periods, approximately longer than 10 s, produce ionospheric responses observable in the ionosphere. The infrasound of periods shorter than about 10 s attenuates below the F2 region heights (~200 km) and is usually not reliably detected by remote sounding [Blanc 1985; Krasnov et al. 2007; Lastovicka et al. 2010; Occhipinti et al. 2010; Rolland et al. 2011].

* Correspondence: jachu@ufa.cas.cz
[1]Institute of Atmospheric Physics CAS, Bocni II/1401, 14131 Prague 4, Czech Republic
Full list of author information is available at the end of the article

Springer

© Chum et al. 2016 **Open Access** This article is distributed under the terms of the Creative Commons Attribution 4.0 International License (http://creativecommons.org/licenses/by/4.0/), which permits unrestricted use, distribution, and reproduction in any medium, provided you give appropriate credit to the original author(s) and the source, provide a link to the Creative Commons license, and indicate if changes were made.

Each strong earthquake represents a unique possibility to study ionospheric response to the relatively well-known source and thus to better understand the coupling between the solid Earth, troposphere, and upper atmosphere and ionosphere. The understanding of ionospheric forcing from below is useful from several reasons. Good understanding of the ionospheric response to acoustic gravity waves excited by tsunamis could be potentially used in the tsunami early-warning systems since the infrasound waves propagate at larger velocities (~330 m/s) than tsunamis (~200 m/s at deep water). So, if the epicenter is sufficiently far in the sea, the related ionospheric disturbances can be detected before the tsunami arrival to the seacoast [Rolland et al. 2010; Liu et al. 2006b; Arai et al. 2011; Shinagawa et al. 2013]. It is, however, crucial to properly distinguish the co-seismic (co-tsunami) ionospheric disturbances from fluctuations caused by other kinds of forcing from below, e.g., acoustic gravity waves from severe weather systems [Nishioka et al. 2013], mountain waves, etc., and from above, e.g., geomagnetic and solar activity [Laštovička 2006; Liu et al. 1996; Šindelářová et al. 2009], and the meteorite falls [Brown et al. 2013] and artificial re-entries [Yamamoto et al. 2011]. A detailed understanding of ionospheric variability and coupling mechanisms is also necessary for the challenging task to correctly recognize/identify potential ionospheric precursors of earthquakes. In this case, if such precursors exist, the coupling between the solid Earth, troposphere, upper atmosphere, and ionosphere is, however, claimed to be based on changes in electric field or changes of global electric circuit owing to radon escape rather than on acoustic gravity waves [Harrison et al. 2010; Liu et al. 2010; Pulinets and Davidenko 2014].

In this paper, we focus on the analysis of co-seismic disturbances in the ionosphere at locations far away from the earthquake epicenter. We show that the coupling mainly occurs via the infrasound waves. We demonstrate that the altitude of observation and altitude profile of plasma density are important factors for the reliable detection of co-seismic perturbation in the ionosphere. These factors might be more important than the horizontal distance from the epicenter.

Measurements and data analysis

Doppler sounding of infrasound waves

Previous Doppler studies of co-seismic perturbation in the ionosphere computed the plasma and neutral particles velocity from the measured Doppler shift f_D from relations that only consider the advective (up and down) motion of the reflecting level and neglect the effect of compression on the observed Doppler shift [e.g., Artru et al. 2004; Liu et al. 2006a]. Chum et al. 2012 applied the theory of Doppler sounding, originally developed for observation of ionospheric response to magneto-hydrodynamic waves [e.g., Sutcliffe and Poole 1989], and introduced a formula that takes into account the effect of compression on Doppler shift and avoids the necessity of integration in general expression for Doppler shift. This paper is based on the work by Chum et al. 2012, but differs in several aspects. It analyzes another earthquake at two different locations simultaneously (two other more distant measurements did not reveal a measurable response). The previous paper analyzed ionospheric signatures of $M = 9.0$ 2011 Tohoku earthquake in the Czech Republic, whereas the current paper deals with ionospheric response of $M = 7.8$ 2015 Nepal earthquake in Taiwan and in the Czech Republic. The previous paper mainly focused on ionospheric signatures from P, S, and SS waves, whereas the current paper analyzes the effects of Rayleigh waves. Also, the time delays between the ionospheric fluctuations and ground surface motions are computed from the root mean square (RMS) values and not from the waveforms. In addition, ray tracing is used to model propagation times instead of simple integration of sound speed along the vertical.

The co-seismic ionospheric variations are investigated by continuous Doppler sounding systems operating in the Czech Republic (~50.3° N, 14.5° E; ~6300 km distance from the epicenter) and Taiwan (~23.9° N, 121.2° E; ~3700 km distance from the epicenter).

The continuous Doppler sounding is based on the measurement of Doppler shift of radio signal that reflects from the ionosphere. The value of the Doppler shift f_D is given by the time change (derivative) of the phase path of the radio signal [Davies et al. 1962; Jacobs and Watanabe 1966]

$$f_D = -2 \cdot \frac{f_0}{c} \frac{d}{dt} \left(\int_0^{z_R} n \cdot dr \right) = -2 \cdot \frac{f_0}{c} \int_0^{z_R} \frac{\partial n}{\partial N} \cdot \frac{\partial N}{\partial t} \cdot dr, \tag{1}$$

where f_0 is the transmitted frequency of the radio wave, c is the speed of light, n is the refractive index for electromagnetic waves, N is the electron (plasma) density, and z_R is the height of reflection. The Doppler system in the Czech Republic currently operates at three different frequencies, $f_0 = 3.59$, 4.65, and 7.04 MHz. The Doppler system in Taiwan operates at a single frequency, $f_0 = 6.57$ MHz.

Vertically propagating radio wave reflects in the region where its refractive index n tends towards zero. Owing to the geomagnetic field, the radio waves propagate in the ionosphere in the L-O mode (ordinary wave) and R-X mode (extraordinary wave) as the cold magnetized plasma supports two propagating modes. The cut-off frequencies (frequencies at which n is zero) for these

modes are given by relations (2) and (3), respectively [e.g., Stix 1962; Gurnett and Bhatacharjee 2005].

$$0 = 1 - \frac{f_p^2}{f_0^2}, \qquad 4\pi f_p^2 = \frac{e^2 N}{\varepsilon_0 m_e}, \tag{2}$$

$$0 = 1 - \frac{f_p^2}{f_0(f_0 - f_{ce})}, \quad 2\pi f_{ce} = \frac{eB}{m_e}, \tag{3}$$

where f_p is the plasma frequency, e is the charge of an electron, ε_0 is the permittivity of the vacuum, m_e is the mass of an electron, f_{ce} is electron cyclotron frequency, and B is the intensity of magnetic field. In other words, the ordinary wave reflects in the region where the local plasma frequency $f_p = f_0$ and the extraordinary waves reflect in the region where the local plasma frequency f_p satisfies (3), which is for

$$f_p = \sqrt{f_0(f_0 - f_{ce})}, \tag{4}$$

We note that the plasma frequency is according to Eq. (2) directly controlled by the electron (plasma) density, which varies with altitude in the ionosphere. The reflection heights can be estimated from the electron density profiles measured by ionosondes from plasma frequencies defined by (2) and (3). Both Doppler sounding systems used in this study are close to an ionosonde.

In the case of oblique (non-vertical) sounding, the reflection occurs when the refractive index $n \to n_H = \sin(\delta)$, where n_H is the horizontal component of the refractive index on the ground and δ is the zenith angle. The exact treatment is based on the solution of Appleton-Hartree equation [e.g., Gurnett and Bhatacharjee 2005]. For small angles δ, the reflection heights for ordinary and extraordinary waves can be to a good approximation simply estimated if the left hand side of Eqs (2) and (3), respectively, is substituted by the quantity $\sin(\delta) = n_H$. The horizontal distance d_H between the used transmitter and receiver is relatively small (d_H ~60 km) compared to the reflection heights both in the Czech Republic and Taiwan, z_R ~145–210 km as is shown later. It is assumed that the reflection points are in the midway between the corresponding transmitter and receiver, so, the zenith angle $\delta = \mathrm{atan}((d_H/2)/z_R)$ ~10°. The sounding can be therefore considered as quasi-vertical. The calculations based on the $\sin(\delta)$ correction show the lowering of reflection heights by ~1–2 km. This lowering is negligible compared to uncertainties of the electron density profile (true heights) measurements, which are ~5–10 km.

Calculating the integral (1) is usually not possible in the experiment since we do not know the plasma density fluctuations $\partial N/\partial t$ along the sounding paths of radio waves. Therefore, a simple formula (5), based on mirror-like approximation, which relates the value of the Doppler shift with the velocity of movement of the reflecting level is often used [e.g. Artru et al. 2004].

$$f_D = -2 f_0 \frac{u_{\mathrm{PV}}}{c}, \tag{5}$$

where u_{PV} is the vertical (radial) velocity of plasma motion. If the reflection is from the heights above ~130 km, plasma is magnetized, which means that plasma can freely move only along the magnetic field lines [e.g., Rishbeth 1997; Kelley 2009]. In that case, the vertical component of plasma velocity u_{PV} owing to collisions with neutral particles moving with vertical velocity w is related by (6)

$$u_{\mathrm{PV}} = w \cdot \sin^2(I), \tag{6}$$

where I is the inclination of geomagnetic field. The Doppler shift is related to vertical velocity of neutral particles w by (7)

$$f_D = -2 f_0 \frac{w \cdot \sin^2(I)}{c}, \tag{7}$$

This formula can only be applied if the gradient of plasma density is very steep and the reflecting level experiences a bulk up and down motion. The infrasound waves, however, cause plasma compressions and decompressions, so the mirror-like approximation is not justified [Chum et al. 2012]. The effect of compression/decompression on the Doppler shift follows from the decomposition of the $\partial N/\partial t$ term in the Eq. (1). Using equation of continuity, we get

$$\frac{\partial N}{\partial t} = -\nabla \cdot (N u_P) = -\nabla N \cdot u_P - N(\nabla \cdot u_P), \tag{8}$$

where u_P is velocity of plasma motion. The first term on the right hand side of Eq. (8) corresponds to advection (up and down motion) of the reflecting level, whereas the second term represents the compression/decompression [Sutcliffe and Poole 1989]. We neglected electron density changes owing to the ionization and recombination. Next, we will investigate one-dimensional case of vertically propagating infrasound. The first term on the right hand side of Eq. (8) is then $\partial N/\partial z \cdot u_{\mathrm{PV}} = \partial N/\partial z \cdot w \cdot \sin^2(I)$, with the help of Eq. (6), and the second term can be rewritten as $N \cdot \partial u_{\mathrm{PV}}/\partial z = N \cdot \partial w/\partial z \cdot \sin^2(I) = i \cdot N \cdot k \cdot w \cdot \sin^2(I) = i \cdot N \cdot 2\pi f_{IS}/c_s \; w \cdot \sin^2(I)$, where $i^2 = -1$, and k, f_{IS}, and c_s represent the infrasound wave vector (number), infrasound frequency and infrasound speed, respectively. Using Eq. (7) and considering the relative inputs of advection and compression to Doppler shift, it is possible to write (under the assumption that the main contribution to the Doppler shift in Eq. (1) is close to the reflection region) an approximation (9) that relates

the vertical velocity of neutral particles w with the observed Doppler shift f_D.

$$w = -f_D \cdot \frac{c}{2f_0 \sin^2(I)} \cdot \frac{\frac{\partial N}{\partial z}}{\left|\frac{\partial N}{\partial z} + iN\frac{2\pi f_{IS}}{c_S}\right|} = f_D \cdot \frac{c}{2f_0 \sin^2(I)} \cdot \frac{\frac{\partial N}{\partial z}}{\sqrt{\left(\frac{\partial N}{\partial z}\right)^2 + \left(N\frac{2\pi f_{IS}}{c_S}\right)^2}}, \quad (9)$$

where the terms $\partial N/\partial z$, N, and c_s are considered at the altitude of observation (reflection of the Doppler signal). Approximation (9) takes into account the relative contributions of advection and compression to the observed Doppler shift, and makes it possible to avoid integration in Eq. (1), which is usually not possible in the experiment, when we do not know the wave field along the sounding paths. Note that for large plasma density gradients, $\partial N/\partial z >> N\cdot(2\pi f_{IS})/c_s$ (sufficiently low frequencies f_{IS} and high propagation speeds c_s) Eq. (9) reduces to the well-known relation (7), as the assumption of mirror-like reflection is satisfied.

The seismic waves propagate along the Earth's surface with supersonic speeds, so the excited infrasonic waves are roughly plane waves with wave vectors deviated from vertical by a small angle α,

$$\sin\alpha = c_{S0}/c_G, \quad (10)$$

where c_{S0} is the speed of sound in the atmosphere above the ground surface and c_G is the speed of seismic wave on the ground surface [Artru et al. 2004; Rolland et al. 2011]. A simplified scheme of geometry is schematically drawn in Fig. 1 (not in scale). The propagation is quasi-vertical since $c_G >> c_{S0}$ as will be shown in the next section.

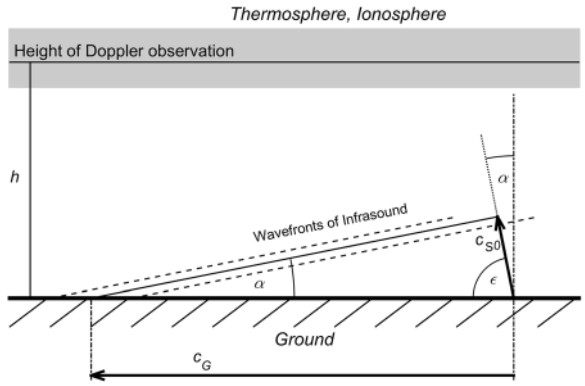

Fig. 1 A scheme of the infrasound generation by seismic waves of observed horizontal velocity c_G. The meaning of variables is as follows: c_{s0} is the initial speed of sound, α is the initial zenith angle of infrasound waves, ε is the initial elevation angle of infrasound wave vector

Measured signals and time delays between the ground surface motion and Doppler record

Figure 2 shows the measured Doppler shifts (red curves) obtained from the original Doppler shift spectrograms as approximations by maxima of spectral intensities at each time, and the vertical velocity v_z of ground surface motion (blue curves) in Taiwan (NACB station) and the Czech Republic (PVCC station) in the time-distance plot. The time is measured from the time of earthquake ($t = 0$ at 06:11:26 UT). The distance from the earthquake epicenter (28.147° N, 84.708° E) is on the vertical, y, axis. To display signals of different amplitudes in one time-distance plot, the fluctuations of Doppler shifts and v_z are normalized by their maximum values. The best Czech Doppler signal was recorded at $f_0 = 4.65$ MHz. Only this signal is shown in Fig. 2 for the Czech Republic station for clarity. The main packet of seismic waves with the highest amplitudes in Fig. 2 corresponds to Rayleigh waves. The related Doppler fluctuations are delayed by 8 min in the Czech Republic (for 4.65 MHz) and by almost 9 min in Taiwan. The analysis of the time delay determination will be discussed later. The speed of propagation of Rayleigh waves estimated from the time distance plot is about 2800 m/s, and the angle α according to relation (10) is about 7° assuming $c_{s0} = 340$ m/s. The long period fluctuations in Doppler records, especially in Taiwan, are most probably owing to atmospheric gravity waves.

We note that our team operates also two other Doppler systems in Hermanus, South Africa, (34.4° S, 19.2° E; ~9800 km distance from the epicenter, $f_0 =$ 3.59 MHz) and in Tucumán, northern Argentina, (26.8° S, 65.2° W; ~17100 km distance from the epicenter, $f_0 =$ 4.63 MHz). In Hermanus, we observed co-seismic fluctuations of Doppler shift on the edge of detectability, about 55 min after the earthquake, which could not be reliably analyzed by methods described further. No co-seismic effect was detected in Tucumán.

Figure 3 presents the dynamic spectra for the signals shown in Fig. 2, which are calculated by the method described by Garces 2013. The plots (a) and (b) display the color-coded power spectral densities of vertical velocities v_z of ground surface motion derived from seismic measurements as a function of time for Taiwan and the Czech Republic. Note the different color scale for these two plots. The peak power spectral density of v_z fluctuation is more than 1000 times larger in Taiwan than in the Czech Republic owing to shorter distance from the earthquake epicenter. Surprisingly, the maximum power spectral densities of Doppler signals measured in Taiwan (c) and the Czech Republic (d) are of about the same value. The frequency ranges of v_z and f_D fluctuations are much more similar for the Czech Republic, with maximum from ~0.035 to ~0.056 Hz, than for Taiwan. As

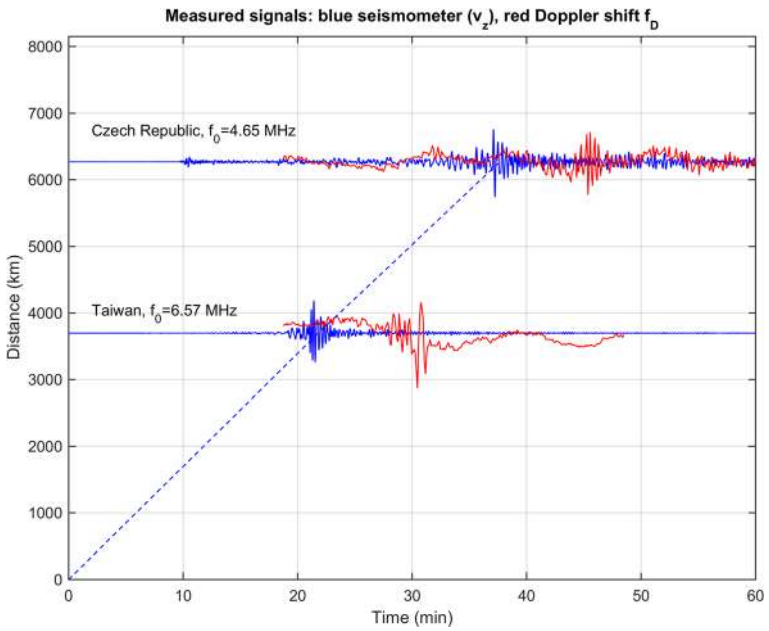

Fig. 2 Vertical component v_Z of the velocity of ground surface movement (*blue*) and observed Doppler shift (*red*) in Taiwan and the Czech Republic (for $f_0 = 4.65$ MHz) as functions of time; time = 0 corresponds to the time of the earthquake (06:11:26 UT). The v_Z values are normalized by their maxima to the same maximum values. The distance from the epicenter is shown on the vertical, y, axis. The *blue dashed line* joins the beginning with maxima of RMS values of v_Z fluctuations

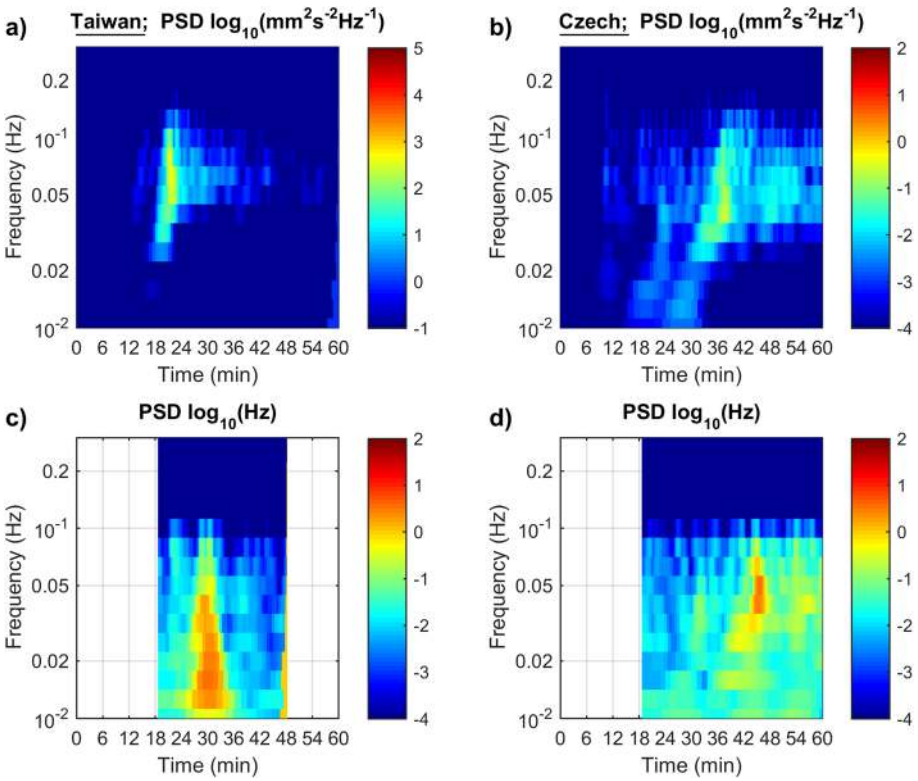

Fig. 3 Spectrograms of the vertical velocity v_Z of the ground surface movement in Taiwan (**a**) and in the Czech Republic (**b**) and spectrograms of the observed Doppler shift in Taiwan (**c**) and in the Czech Republic (**d**) for the time series displayed in Fig. 2. Time = 0 corresponds to the time of the earthquake. Color scales are logarithmic. Note the different color scale for the plots **a** and **b**

will be discussed below, a probable explanation for that is the higher altitude of reflection for Doppler in Taiwan and consequently strong attenuation of higher frequency components of the infrasound waves.

The Rayleigh waves are not well cross-correlated on the ground over distances larger than several tens of km. Consequently, the Doppler signal, which might not be observed directly above the point of seismic measurements due to non-zero zenith angle α (Fig. 1) and owing to non-zero horizontal neutral winds, is not well cross-correlated with the v_z. That is different from the observation of P and S waves and their ionospheric signatures [Chum et al. 2012]. We therefore first calculated RMS values of v_z and f_D and then determined the time delays between the corresponding RMS values. Figure 4a shows the normalized RMS values of v_z fluctuations in Taiwan (solid red) and in the Czech Republic (dashed red), and the normalized RMS values of f_D fluctuations in Taiwan (solid blue) and in the Czech Republic (dashed blue). The displayed RMS values were normalized to the same maximum value for convenient visualization and for more comfortable determination of the time delays. The real RMS amplitudes are displayed in Fig. 4b for completeness. The maximum of RMS(v_z) in Taiwan is in fact 45.5 times larger than the maximum of RMS(v_z) in the Czech Republic, whereas the maximum of RMS(f_D) in Taiwan is only 1.28 larger than the maximum of RMS(f_D) in the Czech Republic, which is consistent with dynamic spectra presented in Fig. 3. The RMS values were computed over the time intervals selected by cosine time window with effective width of 48 s. The time window was subsequently shifted by 6 s, so there is an overlap of 87.5% (=(48–6)/48). Six seconds also correspond to the time resolution of the Doppler shift signal.

The time delays between the normalized RMS values were computed by two different methods: (a) as the time t_C at which the cross-correlation function between the normalized RMS(v_z) and the associated RMS(f_D) has maximum and (b) as the time shift t_S between RMS(v_z) and RMS(f_D) for which the energy of the signal constructed as the sum of the normalized RMS(v_z) and the corresponding normalized RMS(f_D) signals reaches maximum. The times of maxima were refined by quadratic interpolation in both cases. The time delay t_D is then determined as the average value from these two estimates

$$t_D = (t_C + t_S)/2, \tag{11}$$

and the uncertainty of t_D is estimated as

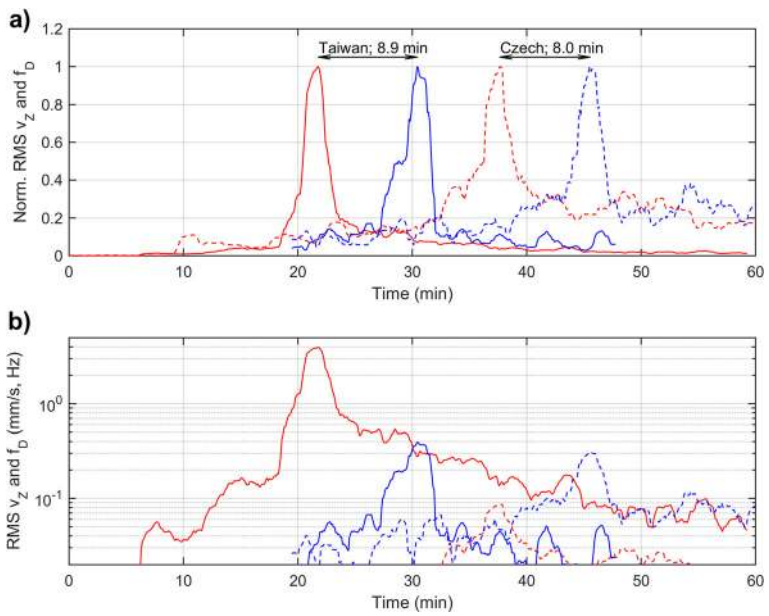

Fig. 4 **a** RMS amplitudes normalized by maximum value of the vertical velocity v_Z of the ground surface movement (*solid red* for Taivan, *dashed red* for the Czech Republic) and of the observed Doppler shifts (*solid blue* for Taiwan, *dashed blue* for the Czech Republic) for the signals displayed in Fig. 2. A low-pass filter with cut-off at ~0.02 Hz was applied before calculating the normalized RMS amplitudes (see the text for more details). Time = 0 corresponds to the time of the earthquake. **b** RMS amplitudes of the vertical velocity v_Z of the ground surface movement (*solid red* for Taiwan, *dashed red* for the Czech Republic) and of the observed Doppler shifts (*solid blue* for Taiwan, *dashed blue* for the Czech Republic) for the signals displayed in Fig. 2

$$\delta(t_D) = \sqrt{(t_C - t_D)^2 + (t_S - t_D)^2 + \Delta t^2}, \quad (12)$$

where $\Delta t = 6$ s is the time resolution of Doppler shift measurements and ensures that the uncertainty is also nonzero for $t_C = t_S$. The time delays and their uncertainties obtained by Eqs. (11) and (12) for the specific Doppler frequencies and locations are presented in the first row in Table 1. The reason for the relatively large uncertainty for the 7.04 Hz signal in the Czech Republic is low Doppler shift, and hence relatively low signal to noise ratio.

Reflection heights

The reflection heights were determined by two independent methods. First, we performed ray tracing for infrasound propagation and search for the altitudes which the infrasound waves reach at times t_D, given in the first row in Table 1. The ray tracing was started with wave vector deviated from vertical by the angle $\alpha \sim 7°$, as discussed above (Eq. 10, and last paragraph of the "Doppler sounding of infrasound waves" section). The sound speed was computed from the atmospheric parameters obtained by the NRLMSISE-00 model for the locations and times of measurements. The neutral winds were neglected for simplicity in what is presented further. We, however, verified that the effect of neutral winds obtained from HWM07 model is negligible for the infrasound travel time to a specific altitude, e.g., the simulated time of infrasound propagation to the altitude of 200 km differed by ~0.1 s when the horizontal wind was considered (the main difference only concerned the horizontal distance travelled by the infrasound waves). Figure 5 shows the ray tracing results for the Czech Republic up to the height of 250 km. Plot (a) shows the ray trajectory in the vertical plane. Plot (b) displays evolution of the elevation angle of wave vector, ε =90°−α, with height (solid line ε, dashed line α). Plot (c) shows the time of propagation versus height. The heights corresponding to the observed time delays t_D are given in row 2 in Table 1. For example, the fluctuations for f_0 = 4.65 MHz were observed at the height $h_M = 163.9 \pm 5$ km. Row 3 in Table 1 gives the sound speed at the modeled height of observation h_M at time t_D. Sound speed as function of height is presented in Fig. 6d for Taiwan (red) and the Czech Republic (blue).

The second method to determine the height of observation is from electron density profile obtained from ionograms measured by ionosondes located in the area of Doppler sounding system (Zhongli in Taiwan, and Pruhonice in the Czech Republic). The reflection height for the ordinary (O) wave is obtained directly as the true height (in electron density profile) that corresponds to the sounding frequency f_0, in accordance with Eq. (2). The reflection height for extraordinary (X) wave is obtained as the true height for the frequency defined by Eq. (4), as discussed in the "Doppler sounding of infrasound waves" section. The ionosonde-derived heights h_I with estimated uncertainties for ordinary (O) and extraordinary (X) mode are given, respectively, in rows 4 and 5 of the Table 1. Figure 6 shows ionograms with calculated true heights of electron density profile measured in Taiwan (Fig. 6a) and the Czech Republic (Fig. 6b) on 25 April 2015 at 06:30 UT and 06:45 UT, respectively. It should be noted that local time (LT) was ~14:30 UT in Taiwan, whereas LT ~7:45 in the Czech Republic. The

Table 1 Measured and simulated parameters in Taiwan and the Czech Republic for the specific frequencies f_0

		Taiwan (f_0 = 6.57 MHz)	Czech Republic (f_0 = 3.59 MHz)	Czech Republic (f_0 = 4.65 MHz)	Czech Republic (f_0 = 7.04 MHz)
1	t_D (s)	532.3 ± 7	449.2 ± 7	480.0 ± 8	548.8 ± 24
2	h_M (km)	201.4 ± 5.1	146.4 ± 4	163.9 ± 5	209.3 ± 17
3	c_S *at* h_M (m/s)	754 ± 11	560 ± 17	626 ± 16	731 ± 32
4	h_I (km) O-mode	229 ± 20	144 ± 10	178 ± 10	230 ± 10
5	h_I (km) X-mode	214 ± 20	102 ± 5	157 ± 10	215 ± 10
6	RMS(f_D)_max (Hz)	0.393	0.172	0.307	0.084
7	w_A max (m/s)	27.7	8.64	11.89	2.14
8	w_{A+C} max (m/s)	0.84 ± 0.42	0.28 ± 0.14	0.41 ± 0.2	0.088 ± 0.044
9	RMS(v_z)_max (m/s)	3.95×10^{-3}	0.087×10^{-3}	0.087×10^{-3}	0.087×10^{-3}
10	w_A/v_z	$(7.16 \pm 0.22) \times 10^3$	$(106 \pm 8.8) \times 10^3$	$(130 \pm 10.2) \times 10^3$	$(30 \pm 7.9) \times 10^3$
11	w_{A+C}/v_z	$(0.22 \pm 0.11) \times 10^3$	$(3.4 \pm 1.7) \times 10^3$	$(4.5 \pm 2.2) \times 10^3$	$(1.2 \pm 0.6) \times 10^3$
12	w/v_z (theor. max)	$(43.7 \pm 3.0) \times 10^3$	$(17.2 \pm 1.8) \times 10^3$	$(25.3 \pm 2.6) \times 10^3$	$(53.2 \pm 13.6) \times 10^3$
13	w/v_z (expected)	$(9.7 \pm 1.7) \times 10^3$	$(14.9 \pm 1.0) \times 10^3$	$(17.4 \pm 0.3) \times 10^3$	$(5.9 \pm 6.2/4.1) \times 10^3$

t_D is the time delay between the seismic wave and observation of the related Doppler shift fluctuations f_D, h_M is the modeled height for the time t_D, c_S is the speed of sound, h_I is the height derived from ionosonde measurements, w_A, w_{A+C} and w is the air particle oscillation velocity computed from Eqs. (7), (9), and (13), respectively (c_{S0} = 334 m/s in the Czech Republic and c_{S0} = 346 m/s in Taiwan, depending on air temperature on ground), and v_z stands for the vertical velocity of ground surface motion

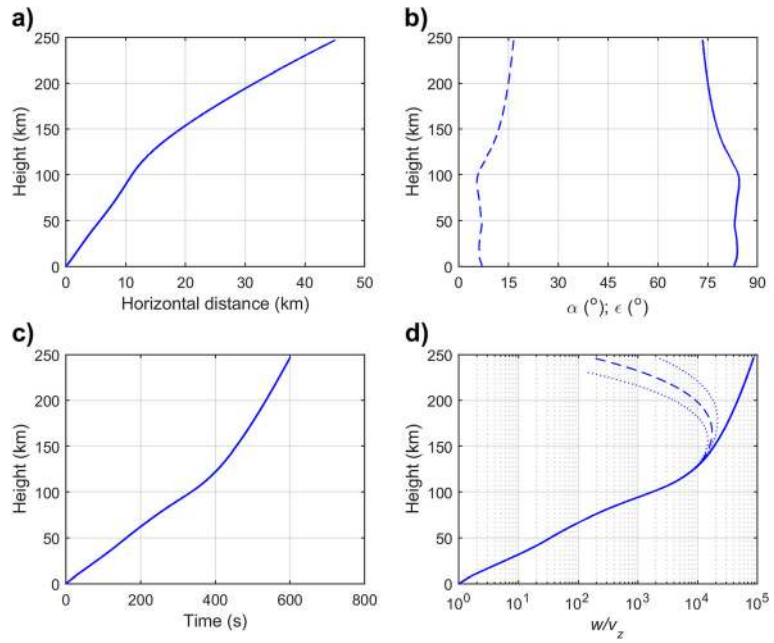

Fig. 5 Infrasound ray tracing results for the Czech Republic; **a** rays in the vertical plane, **b** evolution of elevation angle ε (*solid*) and zenith angle *α* (*dashed*) with height, **c** time of propagation to a specific altitude, **d** modeled w/v_Z ratio (*solid*—theoretical maximum; *dashed*—with attenuation for the central frequency of 0.0455 Hz; *dotted*—with attenuation for the frequencies of 0.035 and 0.056 Hz). See the "Reflection heights" and "Wave amplitudes" sections for more details

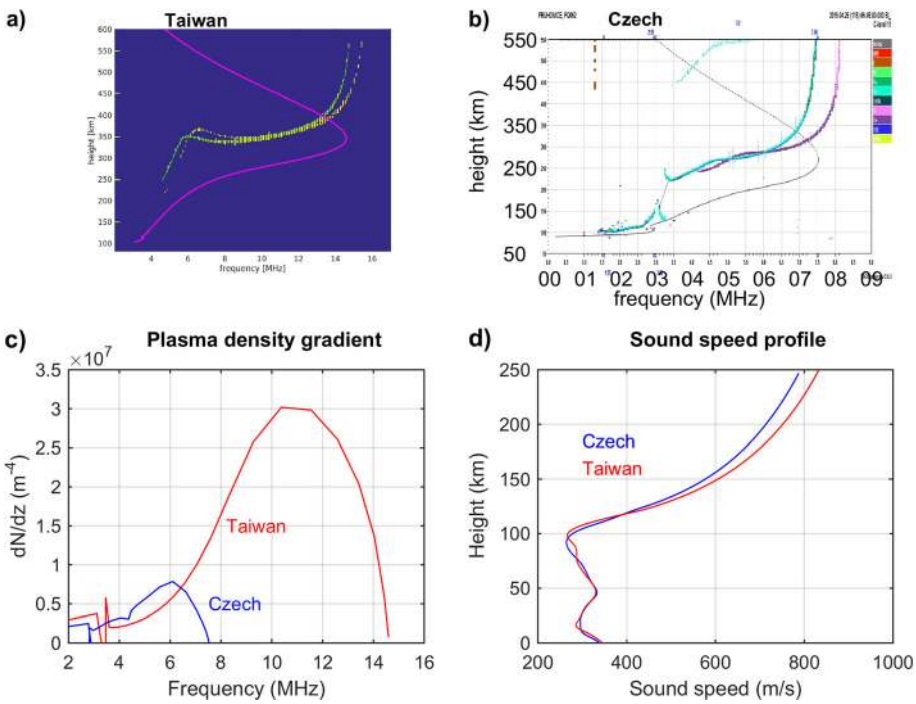

Fig. 6 a Ionogram recorded in Taiwan on 25 April at 6:30 UT with superposed calculated electron density profile (*magenta line*); **b** Ionogram measured in the Czech Republic on 25 April at 6:45 UT with electron density profile (*black line*); **c** plasma density gradient for electron density profile in Fig. 6a), Taiwan (*red*), and profile in Fig. 6b, Czech Republic (*blue*); **d** Sound speed profile for Taiwan (*red*) and the Czech Republic (*blue*)

ionograms in the Czech Republic were obtained by modern digital portable sounder DPS4, and were processed by the dedicated SAO explorer software (version 3.5.1.) which scales the ionograms and computes the electron density profile (Reinisch et al. 2005). The Czech DPS4 sounder is directly in the area of the continuous Doppler sounder (horizontally within several km from reflection points). The ionosonde in Taiwan is about 50 km away from the Doppler sounder, and provides only ionograms in the form of figures. These ionograms—figures of virtual heights—were manually fitted (scaled), and the resulting data were then used as input to the SAO explorer software. The fitting (scaling) from the figures may introduce an additional error (estimated about 10 km). Figure 6c displays the electron density gradients $\partial N/\partial z$ as a function of plasma frequency (sounding frequency) obtained from electron density profiles for Taiwan (red) and the Czech Republic (blue). These values are necessary to apply Eq. (9).

Comparing the h_M heights (row 2) with h_I heights (rows 4 and 5) for the Czech Republic measurements, we deduce that for $f_0 = 3.59$ MHz, the O mode is probably observed, whereas for $f_0 = 4.65$ and $f_0 = 7.04$ MHz, the X mode likely dominated, since $h_M = h_I$ within the estimated uncertainties. It should be noted that for $f_0 =$ 3.59 MHz, the X mode reflected from the E-layer. The Doppler shift of signal reflected from E-layer is usually small (negligible). Moreover, the signal reflected from E-layer often experiences large attenuation (absorption). A comparison of h_M with h_I heights for Taiwan reveals that probably, the X mode was received. We note that the estimated uncertainty of h_I is relatively large for Taiwan since traces in the related ionograms were only detected for frequencies larger than 4.6 MHz, and direct information (measurement) from the bottom-side ionosphere is missing.

Wave amplitudes

Row 6 in Table 1 gives the measured maximum RMS values of f_D fluctuations. We see that the f_D fluctuations in Taiwan and Czech Republic are of the same order for $f_0 = 4.65$ MHz, whereas the RMS(f_D) for $f_0 = 7.04$ MHz is much lower in the Czech Republic. It should be noted that the reflection heights for $f_0 = 4.65$ and $f_0 = 3.59$ MHz in the Czech Republic are lower than reflection height in Taiwan for $f_0 = 6.57$ MHz.

To understand the observed amplitudes of infrasound waves, it is useful to derive the air particle velocities from the observed f_D fluctuations. The air particle velocities computed from the maxima of RMS(f_D) by Eq. (7) are presented in row 7 in Table 1, whereas the air particle velocities calculated by more sophisticated formula (9) are given in row 8. The quantity w_A thus represent air particle velocities computed from the Doppler shift under the approximation of mirror-like reflection, when only advection is considered, whereas the quantity w_{A+C} represent air particle velocities computed from the Doppler shift when both advection and compression are considered in the reflection region. The gradient $\partial N/\partial z$ was obtained from electron density profile measured by nearby ionosondes, and the infrasound frequency of 0.0455 Hz was considered for the calculations by Eq. (9). The signal is, however, not monochromatic; most of the energy is in the frequency range 0.035–0.056 Hz ("Measured signals and time delays between the ground surface motion and Doppler" section). To estimate the uncertainties originated from the usage of single frequency in Eq. (9), we consider the half-width of the 0.035–0.056 Hz frequency range related to the center frequency (~25%). Similarly, from the $\partial N/\partial z$ differences between adjacent ionograms, we estimated the uncertainty of $\partial N/\partial z$ (~25%). These uncertainties then propagate into uncertainties of w_{A+C} values given in row 8 via the application of Eq. (9). The inclination of magnetic field is $I \sim 34.7°$ in Taiwan and $I \sim 65.8°$ in the Czech Republic. According to Eq. (6), the effective vertical plasma motion and hence the measured Doppler shift is about 2.57 times larger (for the same w and $\partial N/\partial z$) in the Czech Republic than in Taiwan. A comparison of the air particle velocities w_A obtained from (7) with velocities w_{A+C} calculated by (9) shows that w_A are more than 20 times larger than w_{A+C}, so the compression mechanism is extremely important, and contributed to the observed Doppler shift f_D more than the advection. We stress that the maximum values of w_A and w_{A+C} are larger than those given in rows 7 and 8 in Table 1 that are related to RMS(f_D) computed over 48 s ("Measured signals and time delays between the ground surface motion and Doppler" section).

Next, we will compare the obtained w_A and w_{A+C} velocities with values expected from simple modeling. It was documented that the air particle oscillation velocities at the ground approach the vertical velocity v_z of ground surface motion [e.g., Watada et al. 2006]. In the case of idealized lossless propagation of infrasound plane wave, the energy density flux $\rho c_s w^2$ across a unit area is conserved, and as the mass density ρ decreases with height, the air particle oscillation velocity w increases according to relation (13)

$$\frac{w}{w_0} = \sqrt{\frac{\rho_0 c_{s0}}{\rho c_s}}, \tag{13}$$

where $w_0 \sim v_z$ is the air particle oscillation velocity at the ground and ρ_0 is the mass density at the ground. The ratio w/w_0 (w/v_z) along the simulated ray trajectory is shown in the plot (d) in Fig. 5 by the solid curve. We note that this ratio represents the maximum possible

value since it corresponds to lossless propagation of the plane wave. In reality, the waves are attenuated and moreover, the rays diverge as the actual waves are not plane waves; consequently, the energy flux is not conserved and decreases with height, so the measured ratios should be lower. Rows 9, 10, and 11 in Table 1 give the maximum of RMS(v_Z), and measured ratio w_A/v_z and w_{A+C}/v_z, respectively. Row 12 in Table 1 presents the maximum theoretical limit given by Eq. (13) obtained from the ray tracing (also an example for the Czech Republic drawn by the solid line in Fig. 5d).

We stress that the measured w_A/v_z ratios are about five times larger than the maximum theoretical limit w/v_z for $f_0 = 4.65$ and $f_0 = 3.59$ MHz in the Czech Republic. This result supports the previous reasoning that in the case of observation of infrasound waves, the compression term cannot be neglected in the Doppler shift analysis and that Eq. (9) gives much more reasonable values, compared to the usually used Eq. (7).

Finally, we also estimated the attenuation of plane wave along its trajectory. The attenuation is based on analytic model described in Section 2.8 of the previous work [Chum et al. 2012]. The analytic model takes into account the classical losses from viscosity and thermal conductivity, and rotational relaxation losses. The model is mainly based on previous studies by Bass et al. 1984 and Sutherland and Bass 2004. The modeled (expected) increase of w/w_0 (w/v_z) is drawn by dashed and dotted curves in Fig. 5d. The dotted curves correspond to the edges of the 0.035–0.056 Hz frequency range, the dashed curve represent the computed ratio for the central frequency of this frequency range. Row 13 in Table 1 gives the expected ratios w/v_z for the central frequency (0.0455 Hz) of the 0.035–0.056 Hz frequency range. The simple analytic model describes relatively well the altitude of maximum ratio w/v_z; note that the maximum ratio w_{A+C}/v_z was measured for $f_0 = 4.65$ MHz at the altitude of ~160 km in agreement with the maximum of calculated w/v_z curve in Fig. 5d.

We note that all the measured ratios w_{A+C}/v_z obtained from (9) are lower than the maximum theoretical limit w/v_z. They are also lower than the modeled ratios w/v_z(expected). That is, however, not surprising. The simple analytic model for attenuation assumes plane wave propagation and does not consider nonlinear effects [e.g., Krasnov et al. 2007]. Maruyama and Shinagawa 2014 also reported that simple analytic solution gives a bit larger amplitude than full-wave modeling. In addition, a part of infrasound energy can be reflected from the bottomside of the thermosphere as the sound speed strongly increases there. The measured ratios w_{A+C}/v_z obtained from (9) seem to be therefore reasonable and do not contradict the theory and previous studies and are in qualitative agreement with expected values.

The dashed curve of the calculated w/v_z in Fig. 5d, more specifically the strong attenuation above ~160 km also explains why the Doppler signal at $f_0 = 4.65$ MHz in the Czech Republic is comparable with the Doppler signal in Taiwan ($f_0 = 6.57$ MHz), though the ratio of ground surface velocities v_z in the Czech Republic and Taiwan is 1/45.5. The reflection height in Taiwan is above 200 km (Table 1), whereas the reflection height for $f_0 = 4.65$ MHz in the Czech Republic is about 160 km (note that the Doppler signal for $f_0 = 7.04$ MHz in the Czech Republic reflecting above 200 km is much smaller than that for $f_0 = 4.65$ MHz). In addition, the same neutral particle velocity w leads to about 2.57 larger vertical plasma motion, and hence a larger Doppler shift f_D (provided the same $\partial N/\partial z$) in the Czech Republic, than in Taiwan, in accordance with Eq. (6) owing to the different inclination angles I. Consequently, the difference between the w_{A+C} or w_A velocities in Taiwan and the Czech Republic is larger, than the corresponding difference between the measured f_D. It is also possible that a nonlinear attenuation of infrasound owing to larger values of w played a role in Taiwan. Moreover, we also cannot exclude that nearby ocean is less effective in generating coherent upward propagating infrasound waves.

Conclusions

We presented analysis of co-seismic perturbations in the ionosphere over the Czech Republic and Taiwan related to seismic waves triggered by the Nepal earthquake on April 25, 2015. It was shown that the ionospheric perturbations, observed by continuous Doppler sounding at large distances from the epicenter (~3700 and ~6300 km), were caused by the infrasound waves generated by the vertical motion of the ground surface. The time delays (~8–9 min) between the ionospheric fluctuations at the heights of observations and ground surface motion are consistent with the calculated times for quasi-vertical propagation of infrasound waves by ray tracing using atmospheric parameters obtained from NRLMSISE-00 model for the locations and times of measurements.

The simulation of infrasound attenuation and the measured values of air particle oscillations (compared with the velocity of ground surface motion) show that the ionospheric disturbances were observed at heights where the infrasound waves were strongly attenuated. Consequently, the observed amplitudes of fluctuations are strongly dependent on the altitude of observation. The observed amplitudes of ionospheric fluctuations can be therefore comparable for different distances from earthquake epicenter, where the source amplitudes of ground surface motion differ by more than one order. Moreover, it was verified that in the case of infrasound observation, the air particle oscillation velocities cannot be calculated from the observed Doppler shifts by a

simple formula based on assumption of mirror-like reflection from a layer that moves up and down. The formula that takes into account electron density and its gradient, and hence the contribution of compression to the observed Doppler shift has to be used. Our analysis shows that the compression mechanism contributed more to the observed Doppler shift than the advection (up and down motion).

Competing interests
None of the authors have competing interest.

Authors' contributions
JCH wrote most of the manuscript and performed most of the data analysis. JYL suggested this work, provided most of the data from Taiwan, and helped with valuable discussion. JL read carefully the manuscript and contributed by improving comments. JF and ZM helped with the ionogram processing and determining of the true heights. JB was responsible for regular operation of Doppler system and primary visualization of Doppler data. YYS helped with Taiwanese data.

Acknowledgements
NASA Community Coordinated Modeling Center is acknowledged for NRLMSISE-00 atmospheric model, http://ccmc.gsfc.nasa.gov/modelweb/atmos/nrlmsise00.html; accessed in September 2015.
The earthquake data archive http://earthquake.usgs.gov/earthquakes, accessed in September 2015, is acknowledged. The Doppler data in the form of spectrograms are available at http://datacenter.ufa.cas.cz/ under the link to Spectrogram archive (accessed in June to September 2015).
The support under the grant 15-07281J by the Czech Science Foundation is acknowledged. This study has been partially supported by the project MOST104-2923-M-008-002-MY3 granted by Ministry of Science and Technology (MOST) to National Central University, Taiwan. The joint project NRF/14/1 of the Czech Academy of Sciences and NRF South Africa made it possible to check South African Doppler data.

Author details
[1]Institute of Atmospheric Physics CAS, Bocni II/1401, 14131 Prague 4, Czech Republic. [2]Institute of Space Science, National Central University, Chung-Li 320, Taiwan.

Received: 10 October 2015 Accepted: 5 February 2016
Published: 17 February 2016

References
Arai N, Iwakuni M, Watada S, Imanishi Y, Murayama T, Nogami M (2011) Atmospheric boundary waves excited by the tsunami generation related to the 2011 great Tohoku-Oki earthquake. Geophys Res Lett 38:L00G18. doi:10.1029/2011GL049146

Artru J, Farges T, Lognonné P (2004) Acoustic waves generated from seismic surface waves: propagation properties determined from Doppler sounding observations and normal-mode modeling. Geophys J Int 158:1067–1077

Avouac JP, Meng L, Wei S, Wang T, Ampuero JP (2015) Lower edge of locked Main Himalayan Thrust unzipped by the 2015 Gorkha earthquake. Nature Geoscience 8:708–711. doi:10.1038/ngeo2518

Bass H, Sutherland ELC, Piercy J, Evans L (1984), Absorption of sound by the atmosphere, in Physical Acoustics, Vol. XVII, Chap. 3., edited by W. P. Mason and R. N. Thurston, pp.145-232, Academic Press, Inc

Blanc E (1985) Observations in the upper atmosphere of infrasonic waves from natural or artificial sources: a summary. Ann Geophysicae 3:673–688

Bolt BA (1964) Seismic air waves from the great 1964 Alaskan earthquake. Nature 202:1095–1096. doi:10.1038/2021095a0

Brown PG, Assink JD, Astiz L, Blaauw R, Boslough MB, Borovička J, Brachet N, Brown D, Campbell-Brown M, Ceranna L, Cooke W, de Groot-Hedlin C, Drob DP, Edwards W, Evers LG, Garces M, Gill J, Hedlin M, Kingery A, Laske G, Le Pichon A, Mialle P, Moser DE, Saffer A, Silber E, Smets P, Spalding RE, Spurný P, Tagliaferri E, Uren D, Weryk RJ, Whitaker R, Krzeminski Z (2013) A 500-kiloton airburst over Chelyabinsk and an enhanced hazard from small impactors. Nature 503:238–241. doi:10.1038/nature12741

Chum J, Hruska F, Zednik J, Lastovicka J (2012) Ionospheric disturbances (infrasound waves) over the Czech Republic excited by the 2011 Tohoku earthquake. J Geophys Res 117:A08319. doi:10.1029/2012JA017767

Davies K, Baker DM (1965) Ionospheric effects observed around the time of the Alaskan earthquake of March 28, 1964. J Geophys Res 70(9):2251–2253. doi:10.1029/JZ070i009p02251

Davies K, Watts J, Zacharisen D (1962) A study of F2-layer effects as observed with a Doppler technique. J Geophys Res 67:2. doi:10.1029/JZ067i002p00601

Donn WL, Posmentier ES (1964) Ground-coupled air waves from the great Alaskan earthquake. J Geophys Res 69:5357–5361

Garces MA (2013) On infrasound standards, Part 1 time, frequency, and energy scaling. InfraMatics 2(2):13–35. doi:10.4236/inframatics.2013.22002

Grandin, R., M. Vallée, C. Satriano, R. Lacassin, Y. Klinger, M. Simoes, and L. Bollinger (2015), Rupture process of the Mw = 7.9 2015 Gorkha earthquake (Nepal): insights into Himalayan megathrust segmentation, Geophys. Res. Lett., 42, doi:10.1002/2015GL066044

Gurnett DA, Bhatacharjee A (2005) Introduction to plasma physics with space and laboratory applications. Cambridge Univ Press, New York

Harrison RG, Aplin KL, Rycroft MJ (2010) Atmospheric electricity coupling between earthquake regions and the ionosphere. J Atmos Sol Terr Phys 72:376–381. doi:10.1016/j.jastp.2009.12.004

Jacobs JA, Watanabe T (1966) Doppler frequency changes in radio waves propagating through a moving ionosphere. Radio Science 1(3):257–264

Kelley MC (2009), The earth's ionosphere, plasma physics and electrodynamics, Second edition, International geophysics series; v 96, Academic Press, Elsevier, ISBN 978-0-12-088425-4.

Kobayashi T, Morishita Y, Yarai H (2015) Detailed crustal deformation and fault rupture of the 2015 Gorkha earthquake, Nepal, revealed from ScanSAR-based interferograms of ALOS-2. Earth, Planets Space 67:201. doi:10.1186/s40623-015-0359-z

Krasnov VM, Drobzheva Y, Lastovicka J (2007) Acoustic energy transfer to the upper atmosphere from sinusoidal sources and a role of non-linear processes. J Atmos Sol Terr Phys 69:1357–1365

Laštovička J (2006) Forcing of the ionosphere by waves from below. J Atmos Sol Terr Phys 68:479–497. doi:10.1016/j.jastp.2005.01.018

Lastovicka J, Base J, Hruska F, Chum J, Sindelarova T, Horalek J, Zednik J, Krasnov V (2010) Simultaneous infrasonic, seismic, magnetic and ionospheric observations in an earthquake epicentre. J Atmos Sol Terr Phys 72:1231–1240. doi:10.1016/jastp.2010.08.005

Le Pichon A, Guilbert J, Vega A, Garcés M, Brachet N (2002) Ground-coupled air waves and diffracted infrasound from the Arequipa earthquake of June 23, 2001. Geophys Res Lett 29(18):1886. doi:10.1029/2002GL015052

Liu JY, Chiu CS, Lin CH (1996) The solar flare radiation responsible for sudden frequency deviation and geomagnetic fluctuation. J Geophys Res 101(A5):10,855–10,862. doi:10.1029/95JA03676

Liu JY, Tsai YB, Chen SW, Lee CP, Chen YC, Yen HY, Chang WY, Liu C (2006a) Giant ionospheric disturbances excited by the M9.3 Sumatra earthquake of 26 December 2004. Geophys Res Lett 33:L02103. doi:10.1029/2005GL023963

Liu J-Y, Tsai Y-B, Ma K-F, Chen Y-I, Tsai H-F, Lin C-H, Kamogawa M, Lee C-P (2006b) Ionospheric GPS total electron content (TEC) disturbances triggered by the 26 December 2004 Indian Ocean tsunami. J Geophys Res 111:A05303. doi:10.1029/2005JA011200

Liu JY, Chen CH, Chen YI, Yang WH, Oyama KI, Kuo KW (2010) A statistical study of ionospheric earthquake precursors monitored by using equatorial ionization anomaly of GPS TEC in Taiwan during 2001–2007. J Asian Earth Sci 39(1–2):76–80

Maruyama T, Shinagawa H (2014) Infrasonic sounds excited by seismic waves of the 2011 Tohoku-oki earthquake as visualized in ionograms. J Geophys Res Space Phys 119:4094–4108. doi:10.1002/2013JA019707

Nishioka M, Tsugawa T, Kubota M, Ishii M (2013), Concentric waves and short-period oscillations observed in the ionosphere after the 2013 Moore EF5 tornado, Geophys. Res. Lett., 40, doi:10.1002/2013GL057963

Occhipinti G, Dorey P, Farges T, Lognonné P (2010) Nostradamus: the radar that wanted to be a seismometer. Geophys Res Lett 37:L18104. doi:10.1029/2010GL044009

Pulinets S, Davidenko D (2014) Ionospheric precursors of earthquakes and global electric circuit. Adv Space Res 53(5):709–723, http://dx.doi.org/10.1016/j.asr.2013.12.035

Reinisch BW, Huang X, Galkin IA, Paznukhov V, Kozlov A (2005) Recent advances in real-time analysis of ionograms and ionospheric drift measurements with digisondes. J Atmos Sol Terr Phys 67:1054–1062

Rishbeth H (1997) The ionospheric E-layer and F layer dynamos—a tutorial review. J Atmos Sol Terr Phys 59:1873–1880

Rolland LM, Occhipinti G, Lognonné P, Loevenbruck A (2010) Ionospheric gravity waves detected offshore Hawaii after tsunamis. Geophys Res Lett 37:L17101. doi:10.1029/2010GL044479

Rolland LM, Lognonné P, Munekane H (2011) Detection and modeling of Rayleigh wave induced patterns in the ionosphere. J Geophys Res 116: A05320. doi:10.1029/2010JA016060

Shinagawa H, Tsugawa T, Matsumura M, Iyemori T, Saito A, Maruyama T, Jin H, Nishioka M, Otsuka Y (2013) Two-dimensional simulation of ionospheric variations in the vicinity of the epicenter of the Tohoku-oki earthquake on 11 March 2011. Geophys Res Lett 40:5009–5013. doi:10.1002/2013GL057627

Šindelářová T, Burešová D, Chum J, Hruška F (2009) Doppler observations of infrasonic waves of meteorological origin at ionospheric heights. Adv Space Res 43:1644–1651

Stix TH (1962) The theory of plasma waves., Mc Graw-Hill Book Comp

Sutcliffe PR, Poole AWV (1989) Ionospheric Doppler and electron velocities in the presence of ULF waves. J Geophys Res 94(A10):13505–13514

Sutherland LC, Bass HE (2004) Atmospheric absorption in the atmosphere up to 160 km. J Acous Soc Am 115:1012–1032

Takai N, Shigefuji M, Rajaure S, Bijukchhen S, Ichiyanagi M, Dhital M, Sasatani T (2016) Strong ground motion in the Kathmandu Valley during the 2015 Gorkha, Nepal, earthquake. Earth, Planets and Space 68:10. doi:10.1186/s40623-016-0383-7

Watada S, Kunugi T, Hirata K, Sugioka H, Nishida K, Sekiguchi S, Oikawa J, Tsuji Y, Kanamori H (2006) Atmospheric pressure chase associated with the 2003 Tokachi-Oki earthquake. Geophys Res Lett 33, L24306. doi:10.1029/2006GL027967

Yamamoto M-Y, Ishihara Y, Hiramatsu Y, Kitamura K, Ueda M, Shiba Y, Furumoto M, Fujita K (2011) Detection of acoustic/infrasonic/seismic waves generated by hypersonic re-entry of the HAYABUSA capsule and fragmented parts of the spacecraft. Publ Astron Soc Japan 63:971–978

Submit your manuscript to a SpringerOpen journal and benefit from:

► Convenient online submission
► Rigorous peer review
► Immediate publication on acceptance
► Open access: articles freely available online
► High visibility within the field
► Retaining the copyright to your article

Submit your next manuscript at ► springeropen.com